Dalton Transactions



PAPER View Article Online
View Journal | View Issue



Cite this: *Dalton Trans.*, 2025, **54**, 14522

Symmetric and asymmetric ligands for Fe^{III} spin crossover – the influence of the C_2 axis

Conor T. Kelly, **D** Emmelyne Cuza, **D** Eoin Pasquetti, *D** Niall Quinn, *Michael Griffin, *D** Peter Nockemann, **D** Helge Müller-Bunz, *D** Julia Bruno-Colmenarez, *D** Solveig Felton, *D** Zoi G. Lada *D** and Grace G. Morgan *D** **

Modulation of the local strain and geometry in Fe^{III} Schiff base complexes has been shown to allow the stabilisation of both the high spin (HS) and low spin (LS) states, along with thermal spin crossover (SCO). Complexes with hexadentate Schiff base ligands can be readily modified by changing the length of the tetraamine backbone linker. We report here 34 complexes of the symmetric [Fe^{III}(R-sal₂232)]⁺ and asymmetric [Fe^{III}(R-sal₂223)]⁺ families, where the former typically support the HS state, along with a handful of SCO examples, and the latter only supports the HS state. Magnetic measurements reveal that one symmetric example, [Fe^{III}(5-I-sal₂232)]ClO₄ **1.5**, undergoes thermal SCO close to room temperature. We compare the structural distortion and spectroscopic properties in these examples, to indentify the factors that influence spin state choice. This reveals the importance of molecular symmetry, by way of a C_2 axis bisecting the complex which is present in the samples which stabilise the LS state so far. The aforementioned example and three others, one reported previously, have short metal-ligand bond lengths suggesting adoption of the LS state coupled with the presence of a C_2 axis. The additional strain in the [Fe^{III}(R-sal₂223)]⁺ complexes due to the asymmetric nature of the backbone results in significantly greater distortion around the Fe^{III} centre which inhibits the stabilisation of the less distorted LS state. Computational analysis of the $[Fe^{III}(5-I-sal_2232)]^+$ and $[Fe^{III}(5-I-sal_2232)]^+$ isomers reveals that the HS state is more stable in the asymmetric [Fe^{III}(5-I-sal₂223)]⁺ species, whereas the energy difference between the HS and LS state for the $[Fe^{III}(5-I-sal_2232)]^+$ cation is sufficiently small to allow for SCO to occur.

Received 31st July 2025, Accepted 4th September 2025 DOI: 10.1039/d5dt01833a

rsc.li/dalton

Introduction

Spin state selection in transition metal ions drives many aspects of their reactivity and function including in redox cycles in biology^{1–4} and catalysis,^{2–7} and in spin crossover systems.^{8–10} Spin states are affected by many factors including the local ligand field strength, coordination constraints and lattice pressure. In Fe^{III} the spin state choices are S = 1/2, S = 3/2 and S = 5/2, with thermal switching typically observed between the S = 1/2 and S = 5/2 states.^{11–13} The potential for thermal spin state switching in Fe^{III} hexadentate Schiff base chelates is well known, with those of the [Fe^{III}(R-sal₂222)]⁺ form first realised,^{14–16} while the related [Fe^{III}(R-sal₂323)]⁺ series is known to favour the S = 1/2

state,^{17–22} where the numbers refer to the lengths of the alkylene chains between each of the nitrogens of the tetramine backbone (*e.g.*, 232 refers to an ethylene, propylene, ethylene linkage). These ligand types can be easily modulated to manipulate the local coordination strain while maintaining a consistent donor set, albeit in different positions. The Fe^{III} complexes shown in Fig. 1 have been studied to date, with the exception of those with the '223' backbone, [Fe^{III}(*R*-sal₂223)]⁺. While Fe^{III} complexes with the '222' and '323' backbones favour SCO and LS respectively, the remaining '232',^{21,23,24} '223', and '333'^{21,25,26} analogues are much less developed.

We have previously reported the '232' complex, [Fe^{III}(4,6-diOMe-sal₂232)]ClO₄,²⁴ which showed an incomplete two-step thermal SCO with complex structural symmetry-breaking phase transitions and associated changes in local point group symmetry. We now extend our structural investigation of Fe^{III} complexes with the '232' series and compare these with the spin state outcomes with the isomeric '223' series in selected examples, reporting 34 new examples. While all the '223' complexes have structural parameters (bond lengths and distortion parameters) consistent with a HS assignment, the '232' series

^aSchool of Chemistry, University College Dublin, Belfield, Dublin 4, Ireland. E-mail: conor.kelly3@ucd.ie, grace.morgan@ucd.ie

bSchool of Chemistry and Chemical Engineering, The QUILL Research Centre, Queen's University Belfast, David Keir Building, Stranmillis Rd, Belfast, BT9 5AG, UK ^cCentre for Quantum Materials and Technologies (CQMT), School of Mathematics and Physics, Queen's University Belfast, Belfast, BT7 1NN, UK

^dDepartment of Chemistry, University of Patras, 26504 Patras, Greece

Dalton Transactions Paper

Fig. 1 Molecular structures of Fe^{III} complexes with hexadentate Schiff base ligands with an $N_4O_2^{2-}$ coordination sphere. Relevant nomenclature is indicated beneath each molecule, whereby the numbers refer to the lengths of the alkylene chains between each of the nitrogens of the tetraamine backbone (e.g., 232 refers to an ethylene, propylene, ethylene linkage). The two ligand types investigated in this work are highlighted in green, with those with the asymmetric 223 ligand, dashed line, reported for the first time in this work.

can stabilise either HS or LS arrangements. We examine the relationship between spin state configuration and ligand in both series using X-ray diffraction, spectroscopic data, and quantum chemistry calculations.

Synthetic procedures

Symmetric complexes 1.1-1.14 were synthesised by a facile one pot Schiff base condensation of a salicylaldehyde and N,N'-bis(2aminoethyl)-1,3-propanediamine followed by complexation with either an Fe^{II} (undergoes aerial oxidation to Fe^{III}) or Fe^{III} salt. Asymmetric complexes 2.1-2.11 were synthesised starting from N-(2-aminoethyl)-N'-(3-aminopropyl)-ethylenediamine drochloride, which was neutralised with triethylamine, followed by the Schiff base condensation with a salicylaldehyde. This was followed by complexation with either an Fe^{II} or Fe^{III} salt. Further synthetic details, including synthetic scheme can be found in section S1 of the SI.

Results and discussion

Single crystal X-ray diffraction (SCXRD)

Structural characterisation of the symmetric [Fe^{III}(Rsal₂232)]⁺ family of complexes. Structural determination of the 1.1-1.14 complexes, reveals an N₄O₂²⁻ coordination sphere around the Fe^{III} centre, with cis-phenolate donors, cis-amine donors and trans-imine donors, similar to that of the earlier [Fe^{III}(R-sal₂222)]⁺ complexes. 14-16 We can utilise the metal-ligand bond lengths to infer the spin state of the Fe^{III} centre, by comparison of values between these samples and similar structures in the literature. 21,23,24 The bond lengths are longer in the HS state, due to lengthening caused by population of the antibonding orbitals. Bond lengths for a selected number of complexes are presented in Table 3, and for all complexes in Table S2.2. Comparison of the bond lengths reveal that in most cases the bond lengths are typically of the order of: Fe-O = 1.91-1.93 Å, Fe-N_{imine} = 2.10-2.12 Å, and Fe-N_{amine} = 2.16-2.24 Å. These lengths are comparable to that of the previously published HS complexes, 1.1a,²¹

1.10a,²¹ and the HS sites in 1.12a.²⁴ There are three outliers, 1.5, 1.12b and 1.13 with noticeably shorter bond lengths, Table 3, which are comparable to the LS site in the previously reported [Fe^{III}(4,6-diOMe-sal₂232)]ClO₄ complex which undergoes two-step SCO.²⁴ In these examples, **1.5**, **1.12b** and **1.13**, and the LS site in **1.12a**, we observe that only half of the cation is in the asymmetric unit, as the complex cation is bisected by a C_2 axis, Fig. 2. The shortened bond lengths in the LS state, allow the ligand to be more symmetrical around the Fe^{III} centre, which is hindered in the more asymmetrically distorted HS examples where often one O-Fe-Namine axis is elongated further than the other. The breaking of the molecular symmetry in the remaining [Fe^{III}(R-sal₂232)]⁺ complexes appears to prevent the complex from accessing the LS state. While the C_2 axis appears necessary for the stabilisation of the LS state, there are a couple of examples where the C_2 axis is present but the HS state is stabilised at the temperature of the diffraction experiment, 1.1a and 1.1b.

We next used structural distortion parameters to quantify the distortion around the $\mathrm{Fe^{III}}$ centres, notably the parameters Σ and Θ , which are commonly used to diagnose the spin state, Table 1.27-29

$$\Sigma = \sum_{i=1}^{12} |\phi_i - 90| \Theta = \sum_{i=1}^{24} |\theta_i - 60|$$

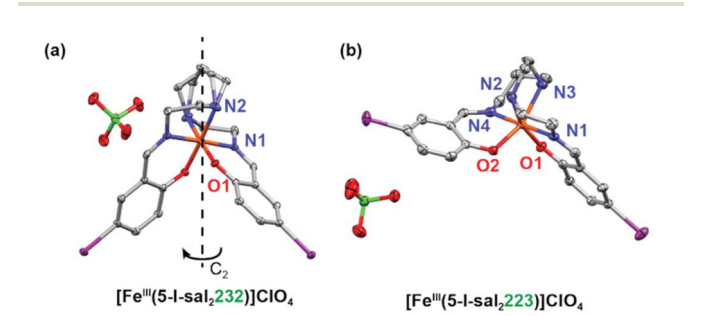


Fig. 2 Structure of isomeric complexes SCO 1.5 (a) and HS 2.4 (b) at 100 K, ellipsoids are drawn at 50% atomic probability. Hydrogen atoms have been omitted for clarity. The asymmetric unit of 1.5 (a) is half of the complex as there is a C_2 axis bisecting the complex.

Table 1 Summary of all complexes with molecular formulae, structural details and structural distortion parameters. Complexes which have been reported previously are indicated with the appropriate citation and CSD Refcode for structural determination

		T^a	. 1-	Σ^c	$\boldsymbol{\Theta}^{c}$		Spin	Space	
	Molecular Formula	(K)	Site ^b	(°)	(°)	$\alpha^c(\circ)$	state ^d	group	Comment
Fe ^{III} (R-sa	l ₂ 232)] ⁺ Family	20-				400	***	D.I	7/ 0 - 0 1 1 1 1 1 1 1 GPD
.1a ^{2ì}	[Fe ^{iff} (sal ₂ 232)]ClO ₄ ²¹	295		116	509	108	HS	Pbcn	$Z' = 0.5$, C_2 axis bisecting cation. CSD Refcode: DABKAS
1b	[Fe ^{III} (sal ₂ 232)]OTf	100	I II	101 80.7	436 260	112 101	HS HS	$P4_2bc$	Two sites, each with a C_2 axis bisecting cation.
1c ²³	$[Fe^{III}(sal_2232)]$	120		73.6	272	86.1	HS	$P22_12_1$	CSD Refcode: HOWHIM
2	$[Mn^{II}Cr^{III}(Br_2An)_3]^e(CH_3CN)_4^{23}$ $[Fe^{III}(5-F-sal_2232)]ClO_4$	100		76.9	254	112	HS	$P2_1/c$	
2 3a	$[Fe^{III}(5-Cl-sal_2232)]ClO_4$	150		92.4	355	104	HS	$P2_1/c$ $P2_1/c$	
3 b	[Fe ^{III} (5-Cl-sal ₂ 232)]BF ₄	100		90.0	341	102	HS	$P2_1/c$	
4a	$[Fe^{III}(5-Br-sal_2232)]ClO_4$	100		88.2	326	105	HS	$P2_1/c$	
4b	[Fe ^{III} (5-Br-sal ₂ 232)]BF ₄	100		84.4	304	103	HS	$P2_1/c$	
5	[Fe ^{III} (5-I-sal ₂ 232)]ClO ₄	100		53.8	141	69.8	LS	C2/c	$Z' = 0.5$, C_2 axis bisecting cation. SCO close to RT.
6	[Fe ^{III} (3,5-diF-sal ₂ 232)]ClO ₄	100		79.4	271	111	HS	$P2_1/n$	
7	[Fe ^{III} (3,5-diCl-sal ₂ 232)]ClO ₄	100		80.5	300	113	HS	$P2_1/n$	
8a	[Fe ^{III} (3,5-diBr-sal ₂ 232)]ClO ₄	100		81.0	301	114	HS	$P2_1/n$	
8b	[Fe ^{III} (3,5-diBr-sal ₂ 232)]NO ₃	100		99.9	364	114	HS	$P2_1/c$	
9a	[Fe ^{III} (3,5-diI-sal ₂ 232)]ClO ₄	100		85.9	319	115	HS	$P2_1/n$	
9b	[Fe ^{III} (3,5-diI-sal ₂ 232)]NO ₃	100	I	97.1	351	116	HS	$P2_1/n$	Two sites
	***		II	118	518	116	HS		
10a ²¹	[Fe ^{III} (3-OMe-sal ₂ 232)]ClO ₄ ²¹	295		84.1	303	96.9	HS	Pccn	CSD Refcode: DABPUR
10b	$[Fe_{III}^{III}(3\text{-OMe-sal}_2232)]NO_3$	100		88.5	325	95.2	HS	Pccn	
10c	[Fe ^{III} (3-OMe-sal ₂ 232)]BF ₄	100		85.5	304	94.3	HS	Pccn	
11	[Fe ^{III} (4-OH-sal ₂ 232)]ClO ₄	293		73.3	248	111	HS	$P2_1/c$	
12a ²⁴	[Fe ^{III} (4,6-diOMe-sal ₂ 232)]ClO ₄ ²⁴	200	_	74.6	302	112	HS	C2/c	Two-step SCO from $HS \rightarrow HS : HS : LS$
		160	I II	54.0 87.5	151 346	108 116	LS HS	C2/c	→ HS: LS: LS. LS site in the HS: HS: LS mixed phase is bisected by a C ₂ axis. CSD Refcode: ELANOV
.12b	[Fe ^{III} (4,6-diOMe-sal ₂ 232)]PF ₆	100		58.9	222	107	LS	C2/c	$Z' = 0.5$, C_2 axis bisecting cation.
12c	[Fe ^{III} (4,6-diOMe-sal ₂ 232)] OTf-0.27H ₂ O	100		73.1	249	96.5	HS	$P\bar{1}$, 2
12d	[Fe ^{III} (4,6-diOMe-sal ₂ 232)]BPh ₄	293		82.8	270	125	HS	$Par{1}$	
13	[Fe ^{III} (5-NO ₂ -sal ₂ 232)]PF ₆	100		64.7	173	103	LS	I2/a	$Z' = 0.5$, C_2 axis bisecting cation.
14	$[\text{Fe}^{\text{III}}(3,5-\text{di}^t\text{Bu-sal}_2232)]\text{ClO}_4$	100		85.0	286	98.8	HS	$P2_1/n$	z oto, oz ana siscering carroni
	ll ₂ 223)] ⁺ Family							1,	
1	[Fe ^{III} (5-F-sal ₂ 223)]NO ₃	100		91.0	317	139	HS	$P2_{1}2_{1}2_{1}$	
2a	Fe ^{III} (5-Cl-sal ₂ 223)]ClO ₄	105		81.2	294	119	HS	Ia	
2b	Fe ^{III} (5-Cl-sal ₂ 223)NO ₃	100		82.7	256	123	HS	Ia	
.3	[Fe ^{III} (5-Br-sal ₂ 223)]ClO ₄	100		81.1	275	121	HS	Ia	
4	[Fe ^{III} (5-I-sal ₂ 223)]ClO ₄	110		82.5	259	122	HS	Ia	
5	[Fe ^{III} (3,5-diBr-sal ₂ 223)]NO ₃	105	I	93.0	330	115	HS	$P\bar{1}$	Two sites
	- 111		II	99.9	429	112	HS	_	
6a	[Fe ^{III} (3-Br-5-Cl-sal ₂ 223)]	105	I	84.7	288	134	HS	$P\bar{1}$	Two sites
	$ClO_4 \cdot 0.25H_2O \cdot 0.25CH_3OH$		II	86.0	301	132	HS	_	
6b	[Fe ^{III} (3-Br-5-Cl-sal ₂ 223)]NO ₃	105	I II	102 93.9	440 332	113 117	HS HS	$P\bar{1}$	Two sites
7	[Fe ^{III} (3-Br-6-OMe-sal ₂ 223)]	115	I	97.5	383	118	HS	$P2_1/c$	Two sites
	ClO ₄ ·0.5CH ₃ OH	4	II	93.9	397	116	HS	DO /	
8 9	[Fe ^{III} (3-OEt-sal ₂ 223)]NO ₃ ·CH ₃ OH [Fe ^{III} (3-MeOMe-5-NO ₂ -sal ₂ 223)]	115 110		83.2 85.3	322 275	125 136	HS HS	$P2_1/c$ $P2_1/c$	
10	ClO ₄ [Fe ^{III} (3-Allyl-sal ₂ 223)]ClO ₄	100	I	82.1	284	114	HS	$Par{1}$	Two sites
	- , - , - , -		II	85.9	289	122	HS		
11	[Fe ^{III} (napsal ₂ 223)]	100		87.8	306	120	HS	$P2_1/c$	
	$ClO_4 \cdot C_2H_3N \cdot 0.33H_2O$								

 $[^]a$ The temperature at which the diffraction experiment was performed. b Where more than one crystallographic site is present the sites are labelled. c The distortion parameters are defined in the main text. d Spin state of the Fe^{III} sites at the temperature of the diffraction experiment was performed. e Where An = anilate.

Dalton Transactions Paper

The Σ parameter is the sum of the deviation of the 12 unique *cis* ligand-metal-ligand angles (ϕ_i) from 90°. The Θ parameter is the sum of the deviation of the 24 unique torsional angles (θ_i) between ligand atoms on opposite triangular faces of the octahedron, Fig. S2.1. In addition, we consider α as the dihedral angle between the least squares planes of the two phenolate rings, as defined by Halcrow et al. 15 with the values summarised in Table 1.

The distortion parameters vary quite widely, dependent on the substitution of the ligand, and also the packing of the molecules in the lattice. The HS complexes have values in the range: $\Sigma = 70^{\circ}-125^{\circ}$; $\Theta = 230^{\circ}-520^{\circ}$; and $\alpha = 85^{\circ}-125^{\circ}$, which are significantly larger than Fe^{III} complexes of the LS [Fe^{III}(Rsal₂323)]⁺ family¹⁸ but of the order of those of HS [Fe^{III}(Rsal₂222)]⁺ complexes. 14-16 Complexes with the '232' and '222' tetraamine backbone are significantly more strained due to the shorter tetraamine backbone than '323', resulting in the cis-orientation of the phenolate donors and increased distortion around the Fe^{III} centre. The structures of '232' with Σ < 65°, Θ < 225° also have bond lengths indicative of the LS state, Fig. 3. While 1.5 has a noticeably smaller α angle than the other complexes reported, there does not appear to be a clear link between this angle and spin state.

The smaller α angle in 1.5 permits stronger hydrogen bonding interactions between the cations and perchlorate anion (N-H···O), Table 2, resulting in a denser packing where hydrogen bonded chains form along the c-axis with the cations arranged pointing the same direction along the chain, Fig. 4(a). Comparing this to the packing in 1.4a, as an example of a HS analogue, reveals a different packing arrangement,

Table 2 Hydrogen bonding interactions for 1.5 SCO and 1.4a HS, with labels corresponding to Fig. 4

Label	d(D-H) (Å)	$d(H\cdots A)$ (Å)	$d(D\cdots A)$ (Å)	∠DHA (°)
1.5 SCO				
1	0.96(3)	2.00(4)	2.957(3)	174(3)
1.4a HS	()	()	()	()
2	0.82(2)	2.18(2)	2.993(2)	167(2)
3	0.84(2)	2.43(2)	3.130(2)	141(2)

where the hydrogen bonding chains are offset with cations of alternating direction along the b-axis, Fig. 4(b). This arrangement in 1.4a is replicated in most of the other complexes in the '232' family, except 1.2, 1.11 and 1.12c which form dimer-

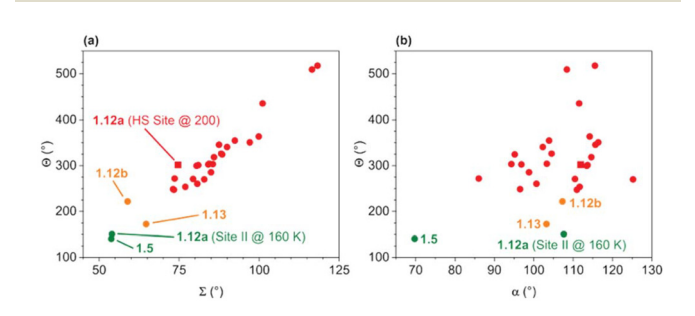


Fig. 3 (a) Comparison of the Σ and Θ distortion parameters for **1.1–1.14**. The sites which show lower values of Σ and Θ exhibit LS or SCO behaviour. The red HS site indicated as a square is one capable of undergoing SCO. (b) Comparison of Θ and α distortion parameters. The sites highlighted in green represent sites assigned as LS, sites in orange represent sites assigned with an equilibrium of HS/LS as full conversion to LS did not occur, and sites in red represent HS.

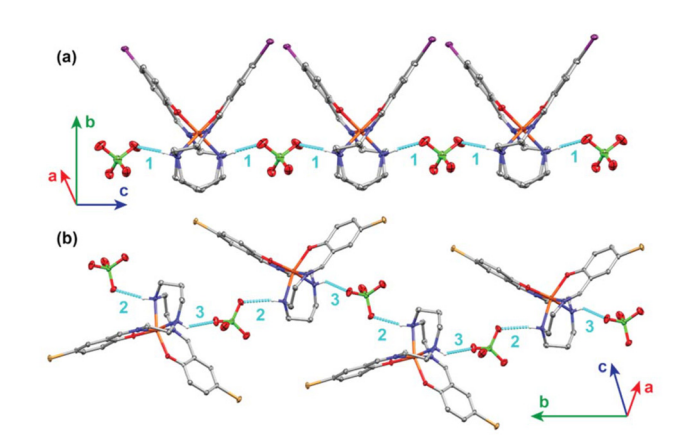


Fig. 4 Partial packing diagram for 1.5 (a) and 1.4a (b) with hydrogen bonding chain formation shown in bright blue. The labels for the hydrogen bonds correspond to the values in Table 2.

Table 3 Summary of bond lengths for selected complexes 1.1a, 1.5, 1.12a, 1.12b, 1.13 and 2.4 at 100 K (unless otherwise indicated)

Complex	1.1a ²¹	1.5	1.12a (160 K) ²⁴		1.12b	1.13	2.4
Site ^a Spin state Bond lengths (Å)	HS	LS	I LS	II HS	LS: HS (mixed) ^b	LS	HS
Fe-O	1.924(3)	1.8805(16)	1.871(3)	1.915(3)	1.8939(13)	1.8921(10)	1.914(6)
	_ ``	_ ` `	_ ``	1.918(3)	_ ` `	_ ` `	1.917(6)
Fe-N _{imine}	2.134(3)	1.9407(18)	1.924(4)	2.077(4)	1.9879(18)	1.9603(12)	2.119(7)
	_ ` `	_ ` ´	_ ` `	2.088(4)	_ ` `	_ ` ´	2.105(7)
Fe-N _{amine}	2.207(3)	2.024(2)	2.002(4)	2.185(4)	2.0888(16)	2.0279(13)	2.204(7)
umme	_	_		2.192(4)	_		2.167(8)

^a Sites are indicated as I and II when more than one crystallographically independent site is present. ^b The bond lengths in this case are slightly longer than expected for a fully LS site.

Paper

like hydrogen bonded units through moieties on the salicylal-dehyde ring, and those with a C_2 axis (1.1a, 1.1b, 1.12a, 1.12b and 1.13). The complexes with a C_2 axis show a similar motif to 1.5 where the cations are arranged pointing the same direction along the hydrogen bonding chain, Fig. S2.2. The combination of the C_2 axis and associated packing arrangement must therefore lead to favourable conditions to promote SCO and stabilise the LS state. Further hydrogen bonding information for 1.1a-1.14 is shown in Table S2.4.

Structural characterisation of the asymmetric [Fe^{III}(Rsal₂223)]⁺ family of complexes. We also report here for the first time complexes with the asymmetric '223' tetraamine backbone, which has the same chain length as the '232' backbone, but no access to C_2 symmetry in the complex due to the position of the propylene linker in this tetraamine. Similarly to the '232' case, the ligand adopts an N₄O₂²⁻ coordination sphere with cis-phenolate donors, cis-amine donors and trans-imine donors. The bond lengths around the Fe^{III} centres are long for all complexes, 2.1-2.11, suggesting the '223' tetraamine backbone has a greater propensity to stabilise the HS state. The asymmetric nature of this ligand means that the Fe-Namine distances are typically longer for those of the amine between the two ethylene linkers than for the amine between the ethylene and propylene linker, e.g. 2.201(9) Å and 2.169(9) Å respectively for 2.4. In addition, the aromatic moiety on the propylene end of the backbone is more distorted. The imine nitrogen, phenolate oxygen and iron atoms deviate from the plane of the aromatic ring as compared to the [Fe^{III}(R-sal₂232)]⁺ examples where the aromatic ring, imine, phenolate oxygen and iron are all almost coplanar.

In the mono-halogenated examples **2.1–2.4** we notice a preference for crystallisation in non-centrosymmetric space groups, Ia (for **2.2–2.4**) and $P2_12_12_1$ (for **2.1**), with those in the Sohncke space group $P2_12_12_1$ having only one of the Δ or Λ isomers of the cationic complex present in the asymmetric unit.

The distortion parameters Σ , Θ , and α are similar in **2.1–2.11**, with values of the same magnitude as the HS sites in the $[\mathrm{Fe^{III}}(R\text{-sal}_2232)]^+$ examples, Table 1 and Fig. 5. Due to the asymmetric nature of this ligand backbone, the α angle is much larger than that of the $[\mathrm{Fe^{III}}(R\text{-sal}_2232)]^+$ examples, with values falling in the 110° to 140° region. This is due to the aforementioned distortion of the aromatic ring on the propylene linker. This increased distortion due to the placement of the propylene linker beside the imine results in the complexes having a preference for stabilisation of the more distorted HS state.

Magnetic measurements

In order to confirm the spin state assignment by SCXRD, and to record the change at different temperatures we performed magnetic susceptibility measurements on those complexes where there was sufficient mass of sample. Plots of $\chi_{\rm M}T$ versus T for 1.5 [Fe^{III}(5-I-sal₂232)]ClO₄ and isomeric 2.4 [Fe^{III}(5-I-sal₂223)]ClO₄ are shown in Fig. 6(a) and (b). The data reveals that 1.5 is LS ($\chi_{\rm M}T=0.48~{\rm cm}^3~{\rm K~mol}^{-1}$) up to ~250 K, with the

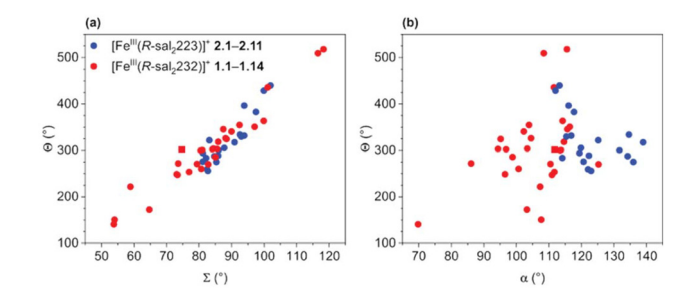


Fig. 5 (a) Comparison of the Σ and Θ distortion parameters for all complexes, with those of the $[\mathrm{Fe^{III}}(R-\mathrm{sal_2232})]^+$ family (1.1–1.14) shown in red, and those of the $[\mathrm{Fe^{III}}(R-\mathrm{sal_2233})]^+$ family (2.1–2.11) shown in blue. The red HS site indicated as a square is one capable of undergoing SCO. (b) Comparison of Θ and α distortion parameters, with the same colour scheme

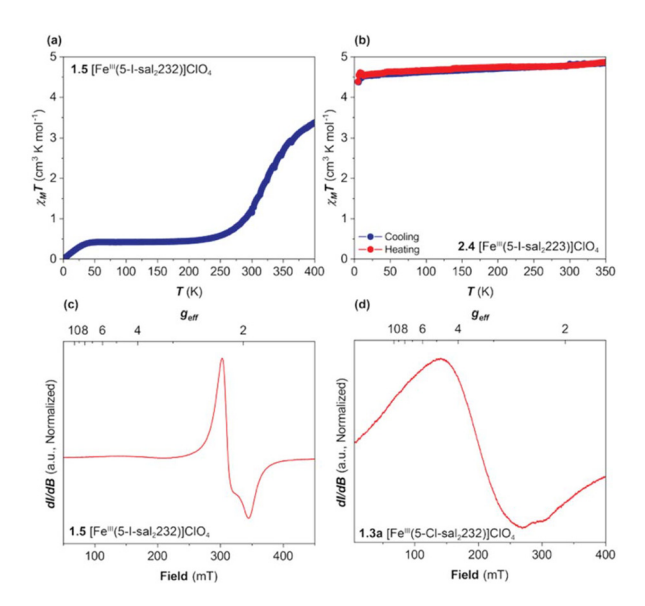


Fig. 6 Plot of $\chi_{\rm M}T$ versus T for 1.5 (a) and 2.4 (b) recorded between 400 K or 350 K and 5 K, at a scan rate of 1 K min⁻¹. EPR spectra for 1.5 (c) and 1.3a (d) recorded on a lightly ground powders at room temperature, using an X-band EPR spectrometer (9.4 GHz).

onset of gradual SCO above this temperature with a maximum value of $\chi_{\rm M}T=3.36~{\rm cm}^3~{\rm K~mol}^{-1}$ at 400 K. For **2.4** the complex is stabilised in the HS state across the measured range with a value of $\chi_{\rm M}T=4.78~{\rm cm}^3~{\rm K~mol}^{-1}$ at 300 K. Additional magnetic measurements for **1.8a**, **1.9a**, **1.10c**, **1.11**, **2.2b**, **2.5**, **2.6a**, **2.6b**, **2.8** and **2.10** are shown in Fig. S3.1, which all show HS values of $\chi_{\rm M}T$ across the measured temperature range.

We also recorded solid state electron paramagnetic resonance (EPR) spectra at room temperature on a lightly ground sample of the SCO sample, **1.5**, and a HS analogue, **1.3a**, Fig. 6(c) and (d). For **1.5** we observe a characteristic axial LS Fe^{III} EPR signal, Fig. 6(c), with an intense resonance centred $g_{\rm eff} \approx 2.1$. A minor resonance is also observed centred close to

Dalton Transactions Paper

 $g_{\rm eff} \approx 4$, which is indicative of the presence of a trace HS component. This matches the observed $\chi_{\rm M}T$ value of 1.03 cm³ K mol⁻¹ observed in the magnetic susceptibility measurement at RT which is slightly higher than the fully LS system. In the case of 1.3a, we observe a broad resonance centred at $g_{\rm eff} \approx 4$, indicating the HS state of this sample.

In solution, room temperature magnetic susceptibility in DMSO-d₆ was determined using Evans' ¹H NMR method and a value of $\chi_{\rm M}T = 3.98~{\rm cm}^3~{\rm K~mol}^{-1}$ was obtained for 1.5 indicating that the complex adopts a spin state closer to that of a pure HS moment $(\chi_{M}T_{\text{spin-only}} (S = 5/2) = 4.375 \text{ cm}^{3} \text{ K mol}^{-1}) \text{ in}$ solution. This suggests that in the absence of the intermolecular interactions and packing effects in the crystal the preferred spin state tends towards HS.

Optical and vibrational spectroscopy

UV-visible spectra were recorded at room temperature on isomeric complexes 1.5 and 2.4 for both solid samples and in acetonitrile solution. The spectra for SCO 1.5 and HS 2.4 are shown in Fig. 7, along with calculated spectra for the respective cationic species (B3LYP/def2-TZVP/D3BJ). For 1.5 we observe differences between the solution measurements and solid state, whereby in solution we observe prominent bands at 240 nm ($\varepsilon_{\text{max}} = 69\,500 \text{ L mol}^{-1} \text{ K}^{-1}$), 304 nm ($\varepsilon_{\text{max}} = 12\,000 \text{ L}$ $\text{mol}^{-1} \text{ K}^{-1}$), 328 nm ($\varepsilon_{\text{max}} = 12\,100 \text{ L mol}^{-1} \text{ K}^{-1}$), and 525 nm $(\varepsilon_{\rm max} = 6100 \text{ L mol}^{-1} \text{ K}^{-1})$. The solution spectra of 1.5 and 2.4 are very similar, which is to be expected as only the backbone of the ligand is changing and not the chromophoric aromatic salicylaldehyde, and the spin state is also remaining consistent, with prominent bands in 2.4 at 240 nm (ε_{max} = 58 300 L $\text{mol}^{-1} \text{ K}^{-1}$), 300 nm ($\varepsilon_{\text{max}} = 10\,500 \text{ L mol}^{-1} \text{ K}^{-1}$), 340 nm (ε_{max} = 8700 L mol⁻¹ K⁻¹), and 512 nm (ε_{max} = 5300 L mol⁻¹ K⁻¹). The solid-state sample of HS 2.4 has bands at similar frequencies as in solution. The difference between the solid-state spectra of HS 2.4 and spin equilibrium LS: HS 1.5 are in line with the spin state assignment from magnetic data.

Raman spectroscopy was recorded on crystals of HS 1.3a, HS 1.4a, SCO 1.5, HS 2.2, HS 2.3, and HS 2.4 at room tempera-

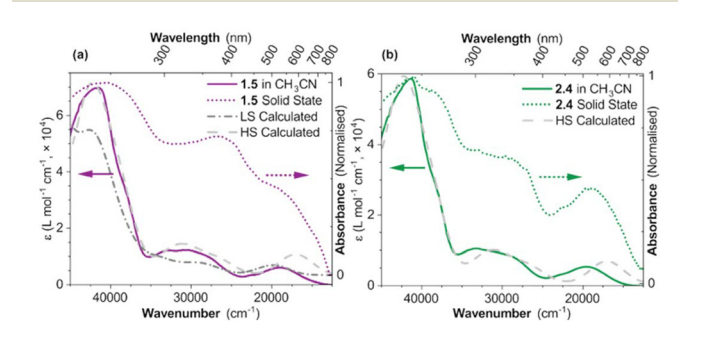


Fig. 7 (a) UV-visible spectra of 1.5 in solution and the solid state along with the calculated spectra for the optimised LS and HS [Fe^{III}(5-Isal₂232)]⁺ cation (B3LYP/def2-TZVP/D3BJ). (b) UV-visible spectra of 2.4 in solution and the solid state along with the calculated spectra for the optimised HS [Fe^{III}(5-I-sal₂223)]⁺ cation (B3LYP/def2-TZVP/D3BJ). All spectra were recorded at room temperature.

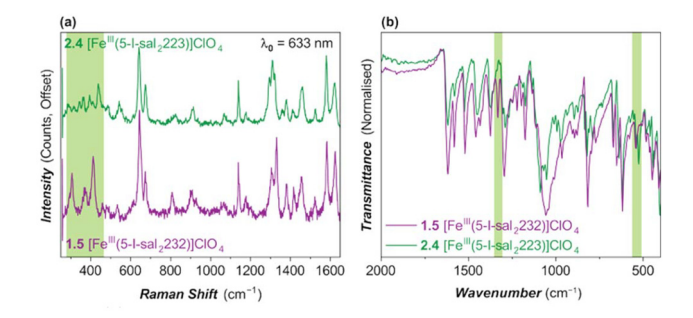


Fig. 8 (a) Raman spectra of 1.5 and 2.4 recorded on crystals of the samples at room temperature. (b) Infrared spectra of 1.5 and 2.4 recorded on crystals of the samples at room temperature. The regions highlighted in green represent where the spectra differ between the two complexes.

ture over a frequency range of 250 cm⁻¹ to 1650 cm⁻¹. Changes in spin state are clearly apparent in the spectra of the isomeric complexes LS: HS 1.5 and HS 2.4, Fig. 8, and are particularly marked in the region between 300-500 cm⁻¹. These are likely due to changes in the ligand to metal bonds as a result of changing spin state and changing backbone. These low-frequency Raman bands at $\sim 304-340$ cm⁻¹ and ~412-436 cm⁻¹ can be attributed to Fe-O stretching and Fe-N stretching vibrations, respectively.32,33 When we compare LS: HS 1.5 with other '232' examples which are HS, Fig. S5.1, a difference in this region is also observed. In the infrared spectrum, differences are observed in the region where metalligand vibrations would be expected, with a shift in one peak from 543 cm $^{-1}$ in 1.5 to 527 cm $^{-1}$ in 2.4. In addition, the peak at 1332 cm⁻¹ in **1.5** is likely due to C-O vibrations shifted to higher wavelength due to the LS state. A strong IR band near 1100 cm⁻¹, attributed to the ν_3 (asymmetric Cl-O stretch) of perchlorate, and a shoulder around 625–640 cm⁻¹ (ν_2 mode) support the presence of non-coordinated ClO₄ ions. 34,35

Quantum chemistry calculations

Quantum chemistry calculations were performed using the ORCA 6.0.1 software package.³⁶ To further understand the energetics in these Fe^{III} complexes we studied the SCO [Fe^{III}(5-Isal₂232)]⁺ and HS [Fe^{III}(5-I-sal₂223)]⁺ cations in more detail. The experimentally obtained molecular coordinates from SCXRD were used as a starting point for the geometry optimisation of the cations, for both the S = 1/2 (LS) and S = 5/2 (HS) states. Comparison of the geometry reveals similarity to the experimentally obtained structures, Table 4. The optimised structure of LS [Fe^{III}(5-I-sal₂232)]⁺ has similar bond lengths and distortions around the Fe^{III} centre to the experimentally obtained structure. While we cannot compare the HS optimised structure directly with experimental data, as the structural data were obtained at 100 K when the complex is fully LS, we note that the bond lengths around the Fe^{III} centre are close to those obtained for HS complexes with different 'R' groups on the phenolate ring, Table 4. One of the most notable differences between the

Table 4 Summary of experimentally determined bond lengths and distortion parameters compared with the parameters for the optimised geometries obtained using TPSSh/def2-TZVP/D3BJ

	LS 1.5	LS Opt	HS Opt	HS 2.4	LS Opt	HS Opt
Bond lengt	hs (Å)					
Fe-O	1.8805(16)	1.890	1.935	1.915(6)	1.870	1.912
	_ ` `	1.886	1.928	1.913(7)	1.910	1.942
Fe-N _{imine}	1.9407(18)	1.936	2.122	2.100(8)	1.974	2.119
	_	1.939	2.122	2.120(9)	1.939	2.133
Fe-N _{amine}	2.024(2)	2.020	2.215	2.169(9)	2.027	2.199
	_	2.055	2.210	2.201(9)	2.029	2.227
Distortion parameters (°)						
Σ	53.80	56.53	79.70	82.46	56.21	91.90
Θ	140.79	149.62	270.33	259.40	170.36	286.52
α	69.76	69.20	113.4	122.03	117.8	130.21

Table 5 Calculated Gibbs free energies (ΔG_{SCO}) upon SCO for the [Fe^{III}(5-I-sal₂232)]⁺ and [Fe^{III}(5-I-sal₂223)]⁺ cations, using both the TPSSh and B3LYP* functional. A positive value means the LS state is favoured and a negative value means the HS state is favoured

	$[\mathrm{Fe^{III}}(5\text{-}\mathrm{I-sal}_2232)]^{\scriptscriptstyle +}$	$\left[\mathrm{Fe^{III}}(5\text{-}\mathrm{I-sal_2}223)\right]^{+}$
$\Delta G_{\text{SCO (HS-LS)}} (\text{kJ mol}^{-1})$		
TPSSh	+36.53	+22.04
B3LYP*	+2.51	-11.11

LS and HS optimised structures of $[Fe^{III}(5\text{-I-sal}_2232)]^+$ is the large change in the α angle between the planes of the phenolate rings, from $\alpha = 69.20^{\circ}$ (LS) to $\alpha = 113.4^{\circ}$ (HS). The optimised structure of $[Fe^{III}(5\text{-I-sal}_2223)]^+$ for the HS state has similar bond lengths and distortions to the experimentally obtained data for 2.4. The LS optimised structure has similar bond lengths to the '232' example, however the phenolate and imine donor adjacent to the propylene linker are quite distorted from the plane of the phenolate ring, perhaps increasing the instability of this spin state in the '223' series.

We use a similar procedure to that benchmarked by Kepp³⁷ and Kulik et al. 38 against FeII and FeIII SCO complexes to determine the Gibb's free energy, ΔG_{SCO} , with the B3LYP* (15% HF exchange) and TPSSh functional, which we also utilised in a previous study of [Fe^{III}(R-sal₂323)]⁺ complexes. ¹⁸ While the absolute values vary depending on the functional used, we can directly compare the ΔG_{SCO} for the $[Fe^{III}(5-I-sal_2232)]^+$ and [Fe^{III}(5-I-sal₂223)]⁺ cations when using the same methods. We observe that the HS state is significantly more stabilised in the [Fe^{III}(5-I-sal₂223)]⁺ cation, which is in agreement with the experimentally obtained data where spectroscopic and structural data reveals that this complex only supports the HS state, Table 5. Comparison of the ΔG_{SCO} to the previously reported values for the LS [Fe^{III}(sal₂323)]⁺ species, ¹⁸ and a reference SCO [Fe^{III}(sal₂222)]⁺ compound show that stability of the LS state decreases with '323' \approx '222' > '232' > '223', which is in line with experimental results for these types of complexes, Table S5.5.

Conclusions

In expanding the series of [Fe^{III}(R-sal₂232)]⁺ from the handful of previous examples, we revealed that of the 25 examples reported, the vast majority are stabilised in the HS state. We show one example where SCO occurs close to room temperature, 1.5, and two other new complexes, 1.12b and 1.13, where crystallographic data indicates the presence of a LS site. In all examples where a LS site has been observed the local symmetry around the Fe^{III} centre resulted in a C_2 axis bisecting the ligand, which appears to be essential for the stability of the less distorted LS state, by virtue of the fact that the decrease in distortion can allow a more symmetric arrangement of the ligand around the Fe^{III} centre. We also report a new family of asymmetric Fe^{III} complexes of the [Fe^{III}(R-sal₂223)]⁺ form. Changes in the local distortion due to the position of the propylene linker (asymmetric '223' arrangement instead of '232') result in these complexes only supporting the HS state. In addition, comparison of the ΔG_{SCO} calculated using DFT showed that the HS state is more energetically favourable in the '223' example, which may be why we only observe the stabilisation of the HS state in these examples.

Experimental details

Synthetic procedures

Reagents were purchased from Merck (Sigma-Aldrich), Fluorochem, TCI Chemicals or VWR and were used without further purification. Complete synthetic details for **1.1–1.14** and **2.1–2.11** can be found in Section S1.

Single crystal X-ray diffraction (SCXRD)

SCXRD data was collected on suitable crystals using a Rigaku Oxford Diffraction SuperNova diffractometer with an Atlas CCD detector. The temperature was controlled using an Oxford Instruments Cryojet. CrysAlisPRO software was used for the data collection, integration, reduction and finalisation.³⁹ An analytical absorption correction based on the shape of the crystal was performed. Structure solution was performed using either direct methods with ShelXS40 or with ShelXT41 and refined by full matrix least-squares on F2 with ShelXL.42 Hydrogen atoms were geometrically constrained and refined riding on the parent atom. Their isotropic displacement parameters were fixed to 1.2 times the parent atom, except for terminal -CH₃ groups where this was 1.5 times the parent atom. All non-hydrogen atoms were refined anisotropically. Further crystallographic details can be found in Section S2. Octahedral distortion parameters were determined using the OctaDist program.⁴³

Magnetic measurements

Magnetic susceptibility measurements were performed using a Quantum Design MPMS-XL SQUID magnetometer (5 T or 7 T) operating between 5 K and 400 K. Magnetic susceptibility was recorded with a field of 0.1 T or 0.5 T on a polycrystalline sample packed in a gelatin capsule at a scan rate of 1 K min⁻¹.

Dalton Transactions Paper

Diamagnetic corrections were applied to correct for the contribution of the diamagnetism of the samples.

Electron paramagnetic resonance (EPR) spectroscopy

EPR spectra were recorded using a Magnettech MS200 X-band (9.4 GHz) spectrometer between 50 and 450 mT with a modulation amplitude of 0.2 mT and a microwave power of 10 mW. Measurements were performed on lightly ground powders of 1.5 and 1.3a.

UV-Visible spectroscopy

UV-visible absorption spectra were acquired using an Agilent Cary 60 UV-Vis spectrophotometer at room temperature. Measurements in solution were conducted in acetonitrile. For solid-state analyses, the samples were finely ground and homogenized with 200 mg of potassium bromide (KBr), then compressed into a transparent pellet using a 15 mm die. The resulting pellet was subsequently mounted onto a solid sample holder for spectral acquisition.

Raman spectroscopy

Raman measurements were performed using the T64000 Horiba Jobin Yvon micro-Raman setup at room temperature. The excitation wavelength for the complex was 632.8 nm, emitted from a He–Ne laser (Optronics Technologies SA Model HLA-20P, 20 mW). The laser power on the sample was 2 mW. The backscattered radiation was collected from a single configuration of the monochromator after passing through an appropriate edge filter (LP02-633RU-25, laser2000, UK, Ltd, Huntingdon, Cambridgeshire, UK). The calibration of the instrument was achieved *via* the standard Raman peak position of Si at 520.5 cm⁻¹. The spectral resolution was 5 cm⁻¹.

Elemental analysis

CHN analysis was performed using an Exeter Analytical CE-440 Elemental Analyser.

Infrared spectroscopy

Infrared spectra were recorded using a Bruker Alpha Platinum ATR-FTIR spectrometer fitted with a diamond anvil.

Evans' method ¹H NMR

Magnetic susceptibility measurements in solution were obtained using Evans' method using an Agilent DD2 500 MHz spectrometer. A standard 5 mm NMR tube containing the sample was fitted with a 3 mm coaxial insert tube containing DMSO- d_6 (6% TMS). The NMR tube was carefully sealed to avoid solvent evaporation. The molar magnetic susceptibility, $\chi_{\rm M}$, for a long cylindrical shape oriented parallel to the magnetic field was calculated according to the equation below, where $\Delta \nu$ is the shift in the frequency of the reference solvent peak in Hz, χ_0 is the molar susceptibility of the solvent, ν_0 is the operating frequency of the spectrometer in Hz, [C] is the concentration of the sample in mol L⁻¹, and

MW is the molecular mass (of either the solvent or sample):

$$\chi_{\rm M} = \chi_0 \frac{{\rm MW}({\rm sample})}{{\rm MW}({\rm solvent})} + \frac{3000 \Delta \nu}{4 \pi \nu_0 [{\rm C}]}$$

Quantum chemistry calculations

Calculations were performed using the ORCA 6.0.1 software. Structural data obtained from SCXRD were used as the starting point for the geometry optimisations. Geometry optimisations were performed using either the B3LYP* 44,45 or TPSSh* 46,47 functional and the triple ζ def2-TZVP basis set* 48 together with the atom-pairwise dispersion correction (D3BJ). Cartesian coordinates of all the optimised geometries can be found in Tables S6.1 and S6.2. Analytical frequencies were calculated at the same level in order to determine that the geometries represented stable energy minima. The thermodynamic properties, $\Delta G_{\rm SCO}$, were computed with T=298.15 K thermodynamic corrections. Calculated UV-visible spectra were determined using TDDFT using the B3LYP functional, which utilised the Tamm-Dancoff approximation (TDA).

Author contributions

C. T. K. - conceptualisation, data curation, formal analysis, investigation, methodology, validation, writing - original draft, writing - review & editing. E. C. - formal analysis, investigation, data curation. E. P. - conceptualisation, formal analysis, investigation. M. G. - formal analysis, investigation. N. Q. investigation. P. N. - investigation, resources. H. M.-B. formal analysis, investigation, data curation. J. B.-C. - formal analysis, investigation. S. F. investigation, resources. L. investigation, methodology, resources. G. G. M. - conceptualisation, funding acquisition, resources, writing - review & editing, supervision, project administration.

Conflicts of interest

There are no conflicts to declare.

Data availability

The data supporting this article have been included as part of the SI. Supplementary information: synthetic details for **1.1–1.14** and **2.1–2.11**; crystallographic details; bond lengths and distortion parameters; additional magnetic measurements; additional UV-visible, infrared and Raman spectra; Cartesian coordinates of the optimised geometries of [Fe^{III}(5-I-sal₂232)]⁺ and [Fe^{III}(5-I-sal₂223)]⁺ cationic species. See DOI: https://doi.org/10.1039/d5dt01833a.

CCDC 2456518–2456538 and 2467729–2467741 contain the supplementary crystallographic data for this paper. $^{52a-ah}$

Acknowledgements

This work was financially supported by Science Foundation Ireland (SFI) with a US-Ireland Award (19/US/3631 to G. G. M.) and a Frontiers for the Future Award (19/FFP/6909 to G. G. M.). The authors wish to thank Mr Rónán Crowley for elemental analysis. A portion of this work has been carried out using the ResearchIT Sonic cluster at University College Dublin which was funded by UCD IT Services and the Research Office.

References

Paper

- I. G. Denisov, T. M. Makris, S. G. Sligar and I. Schlichting, Chem. Rev., 2005, 105, 2253–2278.
- 2 M. Swart and M. Costas, in *Spin States in Biochemistry and Inorganic Chemistry*, 2015, pp. 1–5.
- 3 M. Swart, M. Güell and M. Solà, in *Quantum Biochemistry*, 2010, pp. 551–583.
- 4 M. Swart, Int. J. Quantum Chem., 2013, 113, 2-7.
- 5 M. P. Shaver, L. E. N. Allan, H. S. Rzepa and V. C. Gibson, Angew. Chem., Int. Ed., 2006, 45, 1241–1244.
- 6 M. P. Johansson and M. Swart, *Dalton Trans.*, 2011, 40, 8419–8428.
- 7 J. N. Harvey, R. Poli and K. M. Smith, *Coord. Chem. Rev.*, 2003, **238–239**, 347–361.
- 8 P. Gütlich and H. A. Goodwin, in *Spin Crossover in Transition Metal Compounds I*, ed. P. Gütlich and H. A. Goodwin, Springer Berlin Heidelberg, Berlin, Heidelberg, 2004, pp. 1–47.
- 9 K. S. Murray, in Spin-Crossover Materials, 2013, pp. 1-54.
- 10 A. Bousseksou, G. Molnár, L. Salmon and W. Nicolazzi, *Chem. Soc. Rev.*, 2011, **40**, 3313–3335.
- 11 D. J. Harding, P. Harding and W. Phonsri, *Coord. Chem. Rev.*, 2016, 313, 38–61.
- 12 M. Nihei, T. Shiga, Y. Maeda and H. Oshio, *Coord. Chem. Rev.*, 2007, **251**, 2606–2621.
- 13 P. J. van Koningsbruggen, Y. Maeda and H. Oshio, in *Spin Crossover in Transition Metal Compounds I*, ed. P. Gütlich and H. A. Goodwin, Springer Berlin Heidelberg, Berlin, Heidelberg, 2004, pp. 259–324.
- 14 M. F. Tweedle and L. J. Wilson, J. Am. Chem. Soc., 1976, 98, 4824–4834.
- 15 R. Pritchard, S. A. Barrett, C. A. Kilner and M. A. Halcrow, *Dalton Trans.*, 2008, 3159–3168.
- 16 S. Dorbes, L. Valade, J. A. Real and C. Faulmann, *Chem. Commun.*, 2005, 69–71.
- 17 K. J. Howard-Smith, A. R. Craze, R. Tokunaga, T. Taira, H. Min, M. J. Wallis, D. J. Fanna, S. Hayami and F. Li, *Cryst. Growth Des.*, 2023, 23, 1219–1228.
- 18 C. T. Kelly, M. Griffin, K. Esien, S. Felton, H. Müller-Bunz and G. G. Morgan, *Cryst. Growth Des.*, 2022, 22, 6429–6439.
- 19 R. Kannappan, S. Tanase, I. Mutikainen, U. Turpeinen and J. Reedijk, *Polyhedron*, 2006, **25**, 1646–1654.
- 20 T. Ito, M. Sugimoto, H. Ito, K. Toriumi, H. Nakayama, W. Mori and M. Sekizaki, *Chem. Lett.*, 2006, 12, 121–124.

- 21 S. Hayami, T. Matoba, S. Nomiyama, T. Kojima, S. Osaki and Y. Maeda, *Bull. Chem. Soc. Jpn.*, 1997, 70, 3001–3009.
- 22 C. T. Kelly, S. Dunne, I. A. Kühne, A. Barker, K. Esien, S. Felton, H. Müller-Bunz, Y. Ortin and G. G. Morgan, Angew. Chem., Int. Ed., 2023, 62, e202217388.
- 23 A. Abhervé, M. Clemente-León, E. Coronado, C. J. Gómez-García and M. Verneret, *Inorg. Chem.*, 2014, 53, 12014–12026
- 24 M. Griffin, S. Shakespeare, H. J. Shepherd, C. J. Harding, J. F. Letard, C. Desplanches, A. E. Goeta, J. A. Howard, A. K. Powell, V. Mereacre, Y. Garcia, A. D. Naik, H. Muller-Bunz and G. G. Morgan, *Angew. Chem., Int. Ed.*, 2011, 50, 896–900.
- 25 S. Sundaresan, I. A. Kühne, C. T. Kelly, A. Barker, D. Salley, H. Müller-Bunz, A. K. Powell and G. G. Morgan, *Crystals*, 2019, 9, 19.
- 26 T. Ito, M. Sugimoto, H. Ito, K. Toriumi, H. Nakayama, W. Mori and M. Sekizaki, *Chem. Lett.*, 1983, **12**, 121–124.
- 27 M. G. B. Drew, C. J. Harding, V. McKee, G. G. Morgan and J. Nelson, J. Chem. Soc., Chem. Commun., 1995, 1035–1038.
- 28 P. Guionneau, C. Brigouleix, Y. Barrans, A. E. Goeta, J.-F. Létard, J. A. K. Howard, J. Gaultier and D. Chasseau, C. R. Acad. Sci., Ser. IIc:Chim., 2001, 4, 161–171.
- 29 M. Marchivie, P. Guionneau, J.-F. Létard and D. Chasseau, *Acta Crystallogr., Sect. B:Struct. Sci.*, 2005, **61**, 25–28.
- 30 M. S. Shongwe, S. H. Al-Rahbi, M. A. Al-Azani, A. A. Al-Muharbi, F. Al-Mjeni, D. Matoga, A. Gismelseed, I. A. Al-Omari, A. Yousif, H. Adams, M. J. Morris and M. Mikuriya, *Dalton Trans.*, 2012, 41, 2500–2514.
- 31 J. Tang, J. Sánchez Costa, S. Smulders, G. Molnár, A. Bousseksou, S. J. Teat, Y. Li, G. A. van Albada, P. Gamez and J. Reedijk, *Inorg. Chem.*, 2009, **48**, 2128–2135.
- 32 Z. G. Lada, K. S. Andrikopoulos, A. Chrissanthopoulos, S. P. Perlepes and G. A. Voyiatzis, *Inorg. Chem.*, 2019, 58, 5183–5195.
- 33 Z. G. Lada, A. Chrissanthopoulos, S. P. Perlepes, K. S. Andrikopoulos and G. A. Voyiatzis, *Chem. Commun.*, 2022, 58, 521–524.
- 34 J. L. Pascal, J. Potier, D. J. Jones, J. Roziere and A. Michalowicz, *Inorg. Chem.*, 1985, 24, 238–241.
- 35 K. Nakamoto, in *Infrared and Raman Spectra of Inorganic and Coordination Compounds*, ed. K. Nakamoto, 2008, pp. 149–354.
- 36 F. Neese, Wiley Interdiscip. Rev.: Comput. Mol. Sci., 2022, 12, e1606.
- 37 K. P. Kepp, Inorg. Chem., 2016, 55, 2717-2727.
- 38 V. Vennelakanti, M. G. Taylor, A. Nandy, C. Duan and H. J. Kulik, *J. Chem. Phys.*, 2023, **159**, 024120.
- 39 CrysAlisPRO, Rigaku Oxford Diffraction, Rigaku Corporation, Wroclaw, Poland.
- 40 G. M. Sheldrick, Acta Crystallogr., Sect. A:Found. Crystallogr., 2008, 64, 112–122.
- 41 G. M. Sheldrick, *Acta Crystallogr., Sect. A:Found. Adv.*, 2015, 71, 3–8.
- 42 G. M. Sheldrick, Acta Crystallogr., Sect. C:Struct. Chem., 2015, 71, 3-8.

43 R. Ketkaew, Y. Tantirungrotechai, P. Harding, G. Chastanet, P. Guionneau, M. Marchivie and D. J. Harding, Dalton Trans., 2021, 50, 1086-1096.

Dalton Transactions

- 44 M. Reiher, O. Salomon and B. Artur Hess, Theor. Chem. Acc., 2001, 107, 48-55.
- 45 O. Salomon, M. Reiher and B. A. Hess, J. Chem. Phys., 2002, 117, 4729-4737.
- 46 J. Tao, J. P. Perdew, V. N. Staroverov and G. E. Scuseria, Phys. Rev. Lett., 2003, 91, 146401.
- 47 J. P. Perdew, J. Tao, V. N. Staroverov and G. E. Scuseria, J. Chem. Phys., 2004, 120, 6898-6911.
- 48 F. Weigend and R. Ahlrichs, Phys. Chem. Chem. Phys., 2005, 7, 3297-3305.
- 49 S. Grimme, J. Comput. Chem., 2006, 27, 1787-1799.
- 50 S. Grimme, J. Antony, S. Ehrlich and H. Krieg, J. Chem. Phys., 2010, 132, 154104.
- 51 S. Grimme, J. Chem. Phys., 2013, 138, 244104.
- 52 (a) C. T. Kelly, E. Cuza, E. Pasquetti, N. Quinn, M. Griffin, P. Nockemann, H. Müller-Bunz, J. Bruno-Colmenarez, S. Felton, Z. G. Lada and G. G. Morgan, CCDC 2456518: Experimental Crystal Structure Determination, 2025, DOI: 10.5517/ccdc.csd.cc2ng6jw; (b) C. T. Kelly, E. Cuza, E. Pasquetti, N. Quinn, M. Griffin, P. Nockemann, H. Müller-Bunz, J. Bruno-Colmenarez, S. Felton, Z. G. Lada and G. G. Morgan, CCDC 2456519: Experimental Crystal Structure Determination, 2025, DOI: 10.5517/ccdc.csd. cc2ng6kx; (c) C. T. Kelly, E. Cuza, E. Pasquetti, N. Quinn, M. Griffin, P. Nockemann, H. Müller-Bunz, J. Bruno-Colmenarez, S. Felton, Z. G. Lada and G. G. Morgan, CCDC 2456520: Experimental Crystal Determination, 2025, DOI: 10.5517/ccdc.csd.cc2ng6ly; (d) C. T. Kelly, E. Cuza, E. Pasquetti, N. Quinn, M. Griffin, P. Nockemann, H. Müller-Bunz, J. Bruno-Colmenarez, S. Felton, Z. G. Lada and G. G. Morgan, CCDC 2456521: Experimental Crystal Structure Determination, 2025, DOI: 10.5517/ccdc.csd.cc2ng6mz; (e) C. T. Kelly, E. Cuza, E. Pasquetti, N. Quinn, M. Griffin, P. Nockemann, H. Müller-Bunz, J. Bruno-Colmenarez, S. Felton, Z. G. Lada and G. G. Morgan, CCDC 2456522: Experimental Crystal Structure Determination, 2025, DOI: 10.5517/ccdc.csd. cc2ng6n0; (f) C. T. Kelly, E. Cuza, E. Pasquetti, N. Quinn, M. Griffin, P. Nockemann, H. Müller-Bunz, J. Bruno-Colmenarez, S. Felton, Z. G. Lada and G. G. Morgan, **CCDC** 2456523: Experimental Crystal Structure Determination, 2025, DOI: 10.5517/ccdc.csd.cc2ng6p1; (g) C. T. Kelly, E. Cuza, E. Pasquetti, N. Quinn, M. Griffin, P. Nockemann, H. Müller-Bunz, J. Bruno-Colmenarez, S. Felton, Z. G. Lada and G. G. Morgan, CCDC 2456524: Experimental Crystal Structure Determination, 2025, DOI: 10.5517/ccdc.csd.cc2ng6q2; (h) C. T. Kelly, E. Cuza, E. Pasquetti, N. Quinn, M. Griffin, P. Nockemann, H. Müller-Bunz, J. Bruno-Colmenarez, S. Felton, Z. G. Lada and G. G. Morgan, CCDC 2456525: Experimental Crystal Structure Determination, 2025, DOI: 10.5517/ccdc.csd. cc2ng6r3; (i) C. T. Kelly, E. Cuza, E. Pasquetti, N. Quinn, M. Griffin, P. Nockemann, H. Müller-Bunz, J. Bruno-

Colmenarez, S. Felton, Z. G. Lada and G. G. Morgan, CCDC 2456526: Experimental Crystal Structure Determination, 2025, DOI: 10.5517/ccdc.csd.cc2ng6s4; (j) C. T. Kelly, E. Cuza, E. Pasquetti, N. Quinn, M. Griffin, P. Nockemann, H. Müller-Bunz, J. Bruno-Colmenarez, S. Felton, Z. G. Lada and G. G. Morgan, CCDC 2456527: Experimental Crystal Structure Determination, 2025, DOI: 10.5517/ccdc.csd.cc2ng6t5; (k) C. T. Kelly, E. Cuza, E. Pasquetti, N. Quinn, M. Griffin, P. Nockemann, H. Müller-Bunz, J. Bruno-Colmenarez, S. Felton, Z. G. Lada and G. G. Morgan, CCDC 2456528: Experimental Crystal Structure Determination, 2025, DOI: 10.5517/ccdc.csd. cc2ng6v6; (l) C. T. Kelly, E. Cuza, E. Pasquetti, N. Quinn, M. Griffin, P. Nockemann, H. Müller-Bunz, J. Bruno-Colmenarez, S. Felton, Z. G. Lada and G. G. Morgan, **CCDC** 2456529: Experimental Crystal Structure Determination, 2025, DOI: 10.5517/ccdc.csd.cc2ng6w7; (m) C. T. Kelly, E. Cuza, E. Pasquetti, N. Quinn, M. Griffin, P. Nockemann, H. Müller-Bunz, J. Bruno-Colmenarez, S. Felton, Z. G. Lada and G. G. Morgan, CCDC 2456530: Experimental Crystal Structure Determination, 2025, DOI: 10.5517/ccdc.csd.cc2ng6x8; (n) C. T. Kelly, E. Cuza, E. Pasquetti, N. Quinn, M. Griffin, P. Nockemann, H. Müller-Bunz, J. Bruno-Colmenarez, S. Felton, Z. G. Lada and G. G. Morgan, CCDC 2456531: Experimental Crystal Structure Determination, 2025, DOI: 10.5517/ccdc.csd. cc2ng6v9; (o) C. T. Kelly, E. Cuza, E. Pasquetti, N. Quinn, M. Griffin, P. Nockemann, H. Müller-Bunz, J. Bruno-Colmenarez, S. Felton, Z. G. Lada and G. G. Morgan, CCDC 2456532: Experimental Crystal Determination, 2025, DOI: 10.5517/ccdc.csd.cc2ng6zb; (p) C. T. Kelly, E. Cuza, E. Pasquetti, N. Quinn, M. Griffin, P. Nockemann, H. Müller-Bunz, J. Bruno-Colmenarez, S. Felton, Z. G. Lada and G. G. Morgan, CCDC 2456533: Experimental Crystal Structure Determination, 2025, DOI: 10.5517/ccdc.csd.cc2ng70d; (q) C. T. Kelly, E. Cuza, E. Pasquetti, N. Quinn, M. Griffin, P. Nockemann, H. Müller-Bunz, J. Bruno-Colmenarez, S. Felton, Z. G. Lada and G. G. Morgan, CCDC 2456534: Experimental Crystal Structure Determination, 2025, DOI: 10.5517/ccdc.csd. cc2ng71f; (r) C. T. Kelly, E. Cuza, E. Pasquetti, N. Quinn, M. Griffin, P. Nockemann, H. Müller-Bunz, J. Bruno-Colmenarez, S. Felton, Z. G. Lada and G. G. Morgan, CCDC 2456535: Experimental Crystal Structure Determination, 2025, DOI: 10.5517/ccdc.csd.cc2ng72g; (s) C. T. Kelly, E. Cuza, E. Pasquetti, N. Quinn, M. Griffin, P. Nockemann, H. Müller-Bunz, J. Bruno-Colmenarez, S. Felton, Z. G. Lada and G. G. Morgan, CCDC 2456536: Experimental Crystal Structure Determination, 2025, DOI: **10.5517/ccdc.csd.cc2ng73h**; (*t*) C. T. Kelly, E. Cuza, E. Pasquetti, N. Quinn, M. Griffin, P. Nockemann, H. Müller-Bunz, J. Bruno-Colmenarez, S. Felton, Z. G. Lada and G. G. Morgan, CCDC 2456537: Experimental Crystal Structure Determination, 2025, DOI: 10.5517/ccdc.csd. cc2ng74j; (u) C. T. Kelly, E. Cuza, E. Pasquetti, N. Quinn, M. Griffin, P. Nockemann, H. Müller-Bunz, J. BrunoPaper

Colmenarez, S. Felton, Z. G. Lada and G. G. Morgan, CCDC 2456538: Experimental Crystal Structure Determination, 2025, DOI: 10.5517/ccdc.csd.cc2ng75k; (v) C. T. Kelly, E. Cuza, E. Pasquetti, N. Quinn, M. Griffin, P. Nockemann, H. Müller-Bunz, J. Bruno-Colmenarez, S. Felton, Z. G. Lada and G. G. Morgan, CCDC 2467729: Experimental Crystal Structure Determination, 2025, DOI: 10.5517/ccdc.csd.cc2ntw5k; (w) C. T. Kelly, E. Cuza, E. Pasquetti, N. Quinn, M. Griffin, P. Nockemann, H. Müller-Bunz, J. Bruno-Colmenarez, S. Felton, Z. G. Lada and G. G. Morgan, CCDC 2467730: Experimental Crystal Structure Determination, 2025, DOI: 10.5517/ccdc.csd. cc2ntw6l; (x) C. T. Kelly, E. Cuza, E. Pasquetti, N. Quinn, M. Griffin, P. Nockemann, H. Müller-Bunz, J. Bruno-Colmenarez, S. Felton, Z. G. Lada and G. G. Morgan, **CCDC** 2467731: Experimental Crystal Structure Determination, 2025, DOI: 10.5517/ccdc.csd.cc2ntw7m; (y) C. T. Kelly, E. Cuza, E. Pasquetti, N. Quinn, M. Griffin, P. Nockemann, H. Müller-Bunz, J. Bruno-Colmenarez, S. Felton, Z. G. Lada and G. G. Morgan, CCDC 2467732: Experimental Crystal Structure Determination, 2025, DOI: 10.5517/ccdc.csd.cc2ntw8n; (z) C. T. Kelly, E. Cuza, E. Pasquetti, N. Quinn, M. Griffin, P. Nockemann, H. Müller-Bunz, J. Bruno-Colmenarez, S. Felton, Z. G. Lada and G. G. Morgan, CCDC 2467733: Experimental Crystal Structure Determination, 2025, DOI: 10.5517/ccdc.csd. cc2ntw9p; (aa) C. T. Kelly, E. Cuza, E. Pasquetti, N. Quinn, M. Griffin, P. Nockemann, H. Müller-Bunz, J. Bruno-Colmenarez, S. Felton, Z. G. Lada and G. G. Morgan, CCDC 2467734: Experimental Crystal

Determination, 2025, DOI: 10.5517/ccdc.csd.cc2ntwbq;

(ab) C. T. Kelly, E. Cuza, E. Pasquetti, N. Quinn, M. Griffin,

P. Nockemann, H. Müller-Bunz, J. Bruno-Colmenarez, S. Felton, Z. G. Lada and G. G. Morgan, CCDC 2467735: Experimental Crystal Structure Determination, 2025, DOI: 10.5517/ccdc.csd.cc2ntwcr; (ac) C. T. Kelly, E. Cuza, E. Pasquetti, N. Quinn, M. Griffin, P. Nockemann, H. Müller-Bunz, J. Bruno-Colmenarez, S. Felton, Z. G. Lada and G. G. Morgan, CCDC 2467736: Experimental Crystal Structure Determination, 2025, DOI: 10.5517/ccdc.csd. cc2ntwds; (ad) C. T. Kelly, E. Cuza, E. Pasquetti, N. Quinn, M. Griffin, P. Nockemann, H. Müller-Bunz, J. Bruno-Colmenarez, S. Felton, Z. G. Lada and G. G. Morgan, CCDC 2467737: Experimental Crystal Structure Determination, 2025, DOI: 10.5517/ccdc.csd.cc2ntwft; (ae) C. T. Kelly, E. Cuza, E. Pasquetti, N. Quinn, M. Griffin, P. Nockemann, H. Müller-Bunz, J. Bruno-Colmenarez, S. Felton, Z. G. Lada and G. G. Morgan, CCDC 2467738: Experimental Crystal Structure Determination, 2025, DOI: 10.5517/ccdc.csd.cc2ntwgv; (af) C. T. Kelly, E. Cuza, E. Pasquetti, N. Quinn, M. Griffin, P. Nockemann, H. Müller-Bunz, J. Bruno-Colmenarez, S. Felton, Z. G. Lada and G. G. Morgan, CCDC 2467739: Experimental Crystal Structure Determination, 2025, DOI: 10.5517/ccdc.csd. cc2ntwhw; (ag) C. T. Kelly, E. Cuza, E. Pasquetti, N. Quinn, M. Griffin, P. Nockemann, H. Müller-Bunz, J. Bruno-Colmenarez, S. Felton, Z. G. Lada and G. G. Morgan, CCDC Experimental Crystal 2467740: Structure Determination, 2025, DOI: 10.5517/ccdc.csd.cc2ntwjx; (ah) C. T. Kelly, E. Cuza, E. Pasquetti, N. Quinn, M. Griffin, P. Nockemann, H. Müller-Bunz, J. Bruno-Colmenarez, S. Felton, Z. G. Lada and G. G. Morgan, CCDC 2467741: Experimental Crystal Structure Determination, 2025, DOI: 10.5517/ccdc.csd.cc2ntwky.